Monomer Versus Dimer of Cationic Ir(III) Complexes for Photodynamic Therapy by Two-Photon Activation: A Comparative Study

Agoston Barta, Laetitia Vanwonterghem, Matéo Lavaud, Florian Molton, Guillaume Micouin, Anne-Laure Bulin, A. Banyasz, Jean-Luc Coll, Frédérique Loiseau, Amandine Hurbin, et al.

Monomer *versus* dimer of cationic Ir(III) complexes for Photodynamic therapy by two-photon activation: A comparative study

Agoston Barta,[a] Laetitia Vanwonterghem,[b] Matéo Lavaud,[b] Florian Molton,[a] Guillaume Micouin,[c] Anne-Laure Bulin,[b] Akos Banyasz,[c] Jean-Luc Coll,[b] Frédérique Loiseau,[a] Amandine Hurbin,[b] and Pierre-Henri Lanoë[a*]*

[a] Univ. Grenoble Alpes, CNRS, DCM, 38000 Grenoble, France, E-mail: pierre-henri.lanoe@univ-grenoble-alpes.fr

[b] Univ. Grenoble Alpes, INSERM U1209, CNRS UMR5309, Institute for Advanced Biosciences, 38000 Grenoble, France, E-mail: amandine.hurbin@inserm.fr

[c] Laboratoire de Chimie École Normale Supérieure de Lyon, ENS, CNRS, UCBL UMR 5182, 46 Allée d'Italie, Lyon, 69364 France

[*] Both authors contributed equally

Abstract

Iridium(III) complexes have been recognized as promising candidates for two-photon sensitized photodynamic therapy (PDT). In this context, we report on the study of two complexes, a monomer (**IrL^1**) and a dimer (**Ir$_2$L^2**). Both complexes possess 2-phenylpyridine cyclometallating ligands and a pyridylbenzimidazole derivative as ancillary ligand. In the dimer, the two Ir(III) centers are connected by a non-conjugated bridged bis(pyridylbenzymidazole). We compare the photophysical properties of these complexes. Both display phosphorescent emission in the orange-red part of the visible spectrum, with emissions centered at 610 nm for **IrL^1** and 625 nm for **Ir$_2$L^2**, both exhibiting quantum yields of ~24%. However, **Ir$_2$L^2** turns to be much brighter than the monomer making the dimer four times brighter than **IrL^1**. This trend is consistent under two-photon excitation (TPE) and the singlet oxygen generation quantum yields, indeed the dimer displaying a *figure of merit* (σ_{TPA} x ϕ_Δ) of 40, compared to only 5 for the monomer. Both complexes generate intracellular ROS and exhibit strong phototoxicity upon blue light activation (λ=420 nm), achieving sub-micromolar IC_{50} values in HT29 and A549 cell lines after 24h of incubation. Moreover, with TPE (λ=800 nm), both complexes also generate intracellular ROS and induce cancer cell death.

Keywords: Photodynamic therapy, cancer, Ir complexes, Two-photon excitation, photosensitizers, Reactive Oxygen Species

Introduction

Photodynamic therapy (PDT) represents a powerful therapeutic technique against cancer, bacterial growth and age-related macular degeneration (AMD). It is believed to be the next-generation cancer treatment due to its non-invasiveness, high specificity, and low systemic toxicity.[1–8] PDT involves administering a molecule, called a photosensitizer (PS), to a patient via topical application, tablet, or injection. This compound should ideally accumulate preferentially in the

targeted area and, once a peak concentration is reached, the treatment is initiated by shining light on the area. Upon light excitation, the photosensitizers generate highly cytotoxic singlet oxygen ($^1O_2$), causing cell death to targeted cancer. Despite recent advances in PDT, its clinical application remains limited to early-stage pulmonary, gastric, and esophageal carcinoma, as well as retinal diseases,[9,10] indicating the need for further development of this technique.[1,3,6,11,12] For instance, light penetration is influenced by both the tissue's optical properties and the wavelength used, which in turn affects the amount of light available for absorption by the PS.[13] Intensive research is currently underway to advance PDT and expand its applications, by developing new light sources for example.[14] A key challenge in this effort is the development of new PSs with enhanced properties, such as improved light absorption and higher $^1O_2$ generation quantum yields.

Phosphorescent transition metal complexes are potent candidates as photosensitizers in PDT due to their desirable characteristics, particularly those based on iridium(III): (i) low toxicity,[3,4,12] (ii) ability to penetrate cells (cytoplasm and/or organelles)[3,12,15,16] (iii) efficient absorption of light in the visible range or even in the tissue transparency window (roughly 700-1200 nm), (iv) presence of the heavy atom allowing quasi-quantitative intersystem crossing (ISC) to the triplet state,[17] generally associated with high $^1O_2$ generation, (v) resistance to photobleaching,[17] and (vi) tendency for cancer cells to accumulate lipophilic cations more efficiently compared to healthy cells due to their more negative potential;[18] (vii) chemical versatility of the molecular structure, especially when dealing with the heteroleptic derivatives.[2,19]

One can consider the optimization of a PS for PDT, a fortiori an iridium(III) complex, for PDT, and especially in type II, where the $^1O_2$ generation ability of PSs is critical to the PDT effect. This involves the simultaneous improvement of the amount of light absorbed by the molecule (ε at a given wavelength) and the quantum yield of singlet oxygen generation (ϕ_Δ).[20] This leads to a new coefficient $\varsigma_\Delta = \varepsilon \times \phi_\Delta$,[21,22] which allow to estimate the highest molecular singlet oxygen generation efficiency. ε can be increased by tinkering with the number of chromophores, for example, and ϕ_Δ is directly dependent on the efficiency of the PS intersystem crossing to achieve a maximum triplet state for sensitizing molecular oxygen.[4,20]

Currently, most of the efforts focus on mononuclear complexes[3,12,23–25] where the modifications of the cyclometallating or ancillary ligands allow for tuning cell penetration and both ε and ϕ_Δ. Notably, ε can be significantly enhanced by incorporating organic chromophores into the ligand backbone[26–30] For example, using xanthene in the ancillary ligand backbone results in a mitochondria-targeting PS with high molar absorptivity.[25] Under light irradiation (400–800 nm, 100 mW cm^{-2}), the conjugate induces apoptotic cell death by generating $^1O_2$ with IC_{50} of the order of 5 μM.

The performance of a PS can also be enhanced by using doped nanoparticles[31,32] by synthesizing self-assembled nanoparticules.[33–35] For instance, a series of amphiphilic iridium(III) complexes bearing quaternary ammonium groups were able to self-assemble in vesicle in water buffer. These nanovesicles displayed low dark cytotoxicity, mitochondria-targeted imaging capabilities and induced efficient PDT in tumor cells.[35]

Finally, a limitation of PDT is the use of visible light for photo-activation, which falls out the therapeutic window in the range 600-1300 nm. Working within this range is important as it allows deeper tissues penetration. Two-photon absorption (TPA) involves simultaneous absorption of two photons of the same energy (i.e. same wavelength) and requires an intense light source (focused short pulse laser). TPA enables to work in the tissues transparent zone and provides spatial resolution.[36,37] Ir(III) complexes are suitable for TPA without special molecular engineering.[38]

Therefore, the ideal PS should have a large two-photon cross section (σ_{TPA}) and a high ϕ_{Δ}, leading to the concept of *figure of merit*, defined as σ_{TPA} x ϕ_{Δ}.[39]

In this contribution, we have chosen a molecular approach using a multinuclear iridium(III) complex to increase the light absorption. This approach has proven to be promising to enhance the phosphorescence rate through the enhanced spin–orbit coupling (SOC), especially when both iridium(III) cores shared a common arene, benzene or heterocycle moiety such as pyrimidine, through coordination or cyclometallation.[40–43] Recently, Shafikov *et al* have reported a dinuclear Ir(III) complex, with a rigid bridging chromophoric ligand 2,6-diphenyl[1,3]thiazolo[5,4-f][1,3]benzothiazole displaying a high ε (24 300 $L.mol^{-1}.cm^{-1}$ at 462 nm) and ϕ_{Δ} of 71% in CH_2Cl_2.[41] Our approach is different, as we do not seek to modify the photophysical properties in the multinuclear complex in comparison to the mononuclear. However, a fistful of multimetallic assemblies has been reported for PDT application.[31,33,34,44,45] Recently, we reported the synthesis and characterization of two chiral binuclear iridium(III) complexes (**ΛΛ** and **ΔΔ**) with their diastereomeric mixture (**Ir_2L^2**) and a corresponding racemic monomer.[46] The two complexes **ΛΛ** and **ΔΔ** were optically active, by both the circular dichroism (CD) spectra and their chiral polarized luminescence (CPL). The dimers (**Ir_2L^2**, **ΛΛ** and **ΔΔ**) demonstrate a four-times higher brightness with respect to the monomer (**IrL^1**) and the CPL brightness (B_{CPL}) of the binuclear complexes exhibiting among the highest reported to date for chiral iridium(III) complexes. Phosphorescent dyes allow increased imaging resolution by using a delay between excitation and acquisition, which permits the background fluorescence to be significantly decreased.[47,48] These compounds could be exploited as theragnostic agent for image-guided surgery and cancer PDT,[49,50] we investigated the potential of **IrL^1** and **Ir_2L^2** complexes in PDT. Thus, we present an in vitro study of the binuclear **Ir_2L^2** complex and its mononuclear counterpart **IrL^1** - corresponding to half of **Ir_2L^2** – as photosensitizers for PDT, evaluating their $^1O_2$ generation efficiency (Figure 1).

Synthesis and characterization

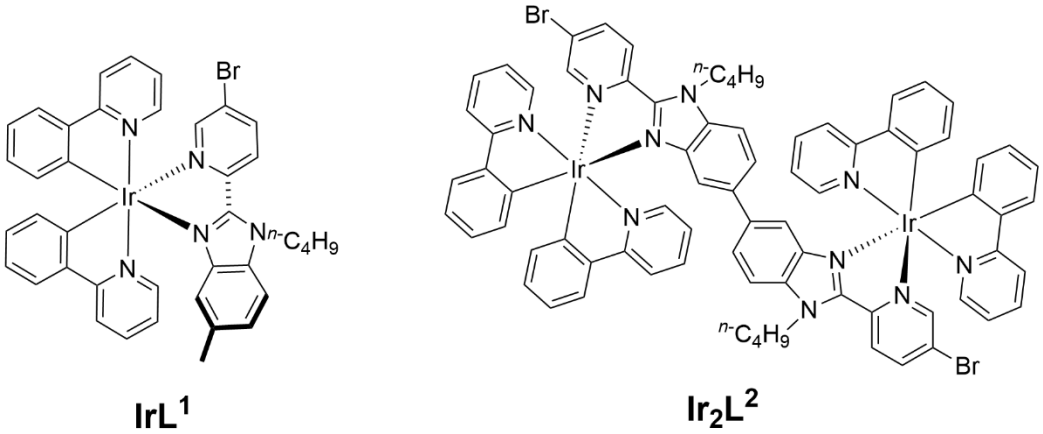

Figure 1 : Cationic Ir(III) complexes isolated with PF_6^- counter ions.

All the compounds were characterized by NMR (^1H and ^{13}C), mass spectroscopy and elemental analysis. The synthesis of both ligand **L^1** and ditopic ligand **L^2**, as well as the final complexes, **IrL^1** and **Ir_2L^2**, was described elsewhere.[46] However, the synthesis schemes, the NMR (^1H and ^{13}C), and mass spectroscopy are displayed in the supporting information.

Photophysical properties

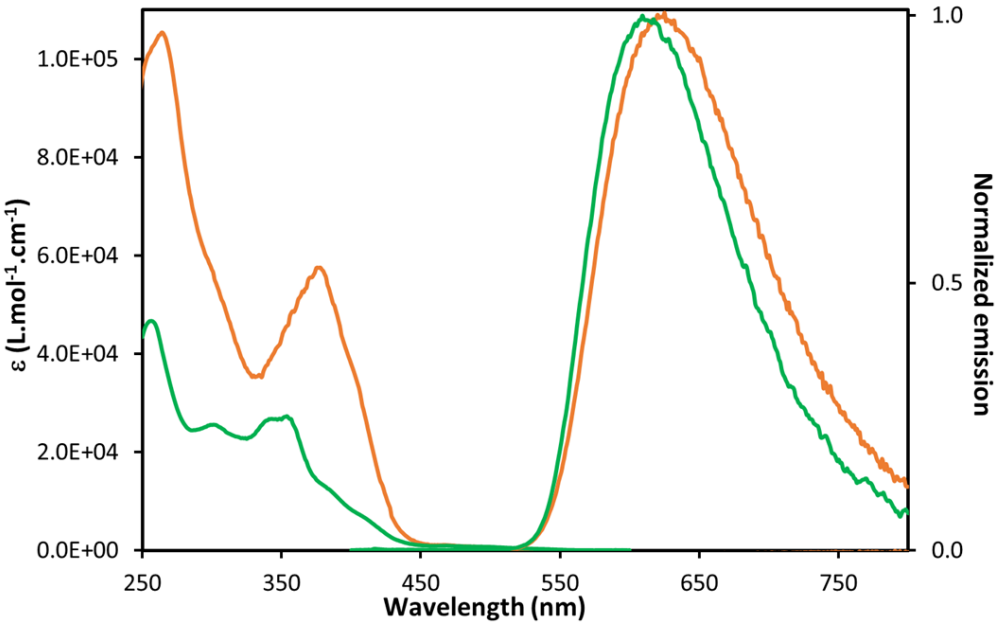

Figure 2 : Absorption and deaerated normalized emission spectra in CH_2Cl_2 of complexes IrL^1 and Ir_2L^2.

Both the emission and absorption spectra have been recorded in dilute CH_2Cl_2 solution under air equilibrated and deaerated conditions (Figure 2 and Table 1). The absorption spectra of iridium complexes could be divided into three spectral domains. In the UV region (250-340 nm), intense absorption bands can be assigned to the spin-allowed π-π* ligand centered transitions (^{1}LC) in both cyclometallating and chelating ligand (i.e. $\mathbf{L^1}$ and $\mathbf{L^2}$). In the second region ranging from 320 nm to 440 nm moderately intense to low absorption bands can be ascribed to mixing of spin allowed metal-to-ligand charge transfer (MLCT) admixed with ligand-to-ligand from the cyclometallating ligand to the π*($\mathbf{L^1}$/$\mathbf{L^2}$) charge transfer (^{1}ILCT) transitions. The third region (see SI) is above 440 nm with very low absorption tail, which can be assigned to the direct spin forbidden absorption from ground state to the ^{3}MLCT/^{3}LLCT excited states, partially allowed thanks to the high spin-orbit coupling constant of the iridium core (ζ = 3909 cm^{-1}).[51] In addition, the bimetallic complex displays a bit more than the double of the absorbance of complex $\mathbf{IrL^1}$. For example, the highest absorption band has a molar extinction coefficient of 46.3 × 10^3 M^{-1} cm^{-1} for $\mathbf{IrL^1}$ and 98.7 x 10^3 M^{-1} cm^{-1} for $\mathbf{Ir_2L^2}$. The bimetallic complex displays higher molar absorptivity in the visible region of the spectrum, and the bands corresponding the (M/L)LCT are red-shifted (ΔE = 1853 cm^{-1}), from 355 nm to roughly 380 nm, for $\mathbf{IrL^1}$ and $\mathbf{Ir_2L^2}$, respectively. Such a feature has been previously observed.[52] Finally, the absorption tail above 440 nm displays a molar absorptivity that corresponds almost exactly to the addition of the absorbance spectra of two $\mathbf{IrL^1}$ units, pointing out that there is no electronic coupling in the ground state between the two parts of the dimer, which would be the case with a rigid bridging ligand.[53,54]

Both complexes display an orange-red color, with an emission maximum in the range 610-625 nm, which can be ascribed to phosphorescence considering the lifetimes of hundreds of ns and the sensitivity to oxygen. In comparison with previously reported complexes bearing 2-2'-pyridylbenzimidazole, the introduction of bromide atoms in position 5' of the pyridyl moiety leads to a somewhat strong bathochromic shift of 30 nm and 45 nm, for the monometallic and bimetallic complexes respectively.[55–57] The photoluminescence quantum yields remain high with respect to the energy gap law (i.e. nonradiative transitions become increasingly important with red emitters).[58] In comparison to $\mathbf{IrL^1}$, $\mathbf{Ir_2L^2}$ displays a slight redshift (λ_{max}= 610 nm and 625 nm, respectively). However,

considering the emission energy difference of only 0.05 eV, this redshift is negligible, suggesting that the ground state of **L^2** may deviate slightly from the expected planar structure. The emission spectra obtained in rigid matrix at low temperature (77 K, Figure S7) display a rigidochromism, which is typical of transition metal complexes submitted to a rigidification of the environment by a decrease of the temperature. Together, the rigidochromism at low temperature and the broad emission spectra at room temperature observed for both complexes allow to conclude the phosphorescence emanates from the radiative deactivation of the ^{3}MLCT* state to the ground state. The brightness ($B_{380\ nm} = \varepsilon \times \phi$)[59] takes in account both absorption of light and ϕ, since a high quantum yield coupled with low absorption of light would yield a poorly luminescent active material.[20,60] The bimetallic derivative **Ir_2L^2** displays a four times higher brightness value than the monometallic, with values of B = 13.0 x 10^3 and B = 3.0 x 10^3, respectively. This demonstrates that **Ir_2L^2** displays advantageous emission properties in comparison with **IrL^1**.

Table 1 : Absorption and emission data recorded in CH_2Cl_2, singlet oxygen generation quantum yields in $CHCl_3$ and molecular singlet oxygen generation efficiency.

Complex	Absorption (x10^4 L.mol^{-1}.cm^{-1})	λ_{em} /nm	ϕ [a], [b] [air]	τ[b]/ns [air]	$k[O_2]$/L.mol^{-1}.s^{-1} (x 10^9)	ϕ_Δ[c]	B[d] x 10^3 /mol^{-1}.cm^{-1}	ς_Δ[e] ($\varepsilon \times \phi_\Delta$) x 10^3	*Figure of merit*[f] ($\sigma_{TPA} \times \phi_\Delta$)	Electrochemical properties[g] (V)	
										E^{red}	E^{ox}
IrL^1	257 (4.7), 302 (2.6), 340 (2.6), 355 (2.7), 388 (1.1), 416 (0.5), 470 (0.1),	610	0.23 [0.08]	918 [228]	0.8	0.66	3.0	5	5	-1.56^{irr}	0.95
Ir_2L^2	267 (9.8), 303 (5.1), 335 (3.3), 378 (5.5), 470 (0.2)	625	0.24 [0.07]	783 [242]	1.4	0.78	13.0	24	40	-1.55^{irr}	0.96

[a] $[Ru(bpy)_3]^{2+}$ in H_2O was used as reference, [b] dearated, [c] singlet oxygen generation quantum yield obtained in $CHCl_3$ from Stern-Volmer plot using phenalenone as standard with Φ_Δ = 0.98 in $CHCl_3$, [d] molecular brilliance B = ε x Φ (eq. 1), ε at 380 nm [e] ς_Δ, molecular singlet oxygen generation efficiency with ε at 420 nm. [f] *Figure of merit* is calculated at 780 nm as Ti:sapphire laser operating at 780 nm is the most commonly used laser for *in vivo* applications. [g] Potentials obtained by cyclic voltammetry using Bu_4NPF_6 (0.1 M) as the supporting electrolyte in CH_3CN. Potentials are given relative to the Ag^+/Ag couple (Reference electrode ANE2, $AgNO_3 = 10^{-2}$ M) measured under the same conditions.

Two-photons absorption

The two-photons absorption cross-sections, σ_{TPA} of **IrL^1** and **Ir$_2$L^2** were measured by the two-photons excited fluorescence (TPEF) technique. Figure 3 presents the results of the TPEF measurement for **IrL^1** and **Ir$_2$L^2**. First, we assessed the emission intensity as a function of the excitation power (Figure 3a). Subsequently, a nonlinear regression analysis was performed to ascertain the order of the power dependence. Notably, the slope values were determined to be 1.97 for **IrL^1** and 1.91 for **Ir$_2$L^2**, indicating that in both cases two-photons absorption is the origin of the observed emission. Figure 3b illustrates the one- and two-photons absorption spectra of **IrL^1** and **Ir$_2$L^2**. For comparison the two-photons absorption cross-section values are normalized by the number of metal centers (n_{Ir}), the one-photon absorption spectra are normalized so that their maxima match with their two-photon counterparts. The shapes of the one-and two-photons absorption spectra show a significant overlap for both compounds. Like the linear absorption, the two-photons absorption spectrum of **Ir$_2$L^2** exhibits a pronounced red shift in comparison to **IrL^1**, peaking at approximately 740 nm. A relatively weak though significant cross section is measured for **IrL^1** with σ_{TPA} maximum of roughly 18 G.M at 700 nm, and in stark contrast **Ir$_2$L^2** exhibits a higher σ_{TPA} maximum of 80 G.M. at 740 nm. These absolute values of σ_{TPA} are comparable with those observed for similar Ir(III) complexes, especially those without specific ligand engineering for TPE.[4,12,61–63] Intriguingly, the red shift is accompanied by a remarkable more-than-doubled enhancement in the two-photon absorption cross section per Ir-center for **Ir$_2$L^2** as compared to **IrL^1**. Once again, the use binuclear complex displays advantageous properties, that surpass the mononuclear counterpart.

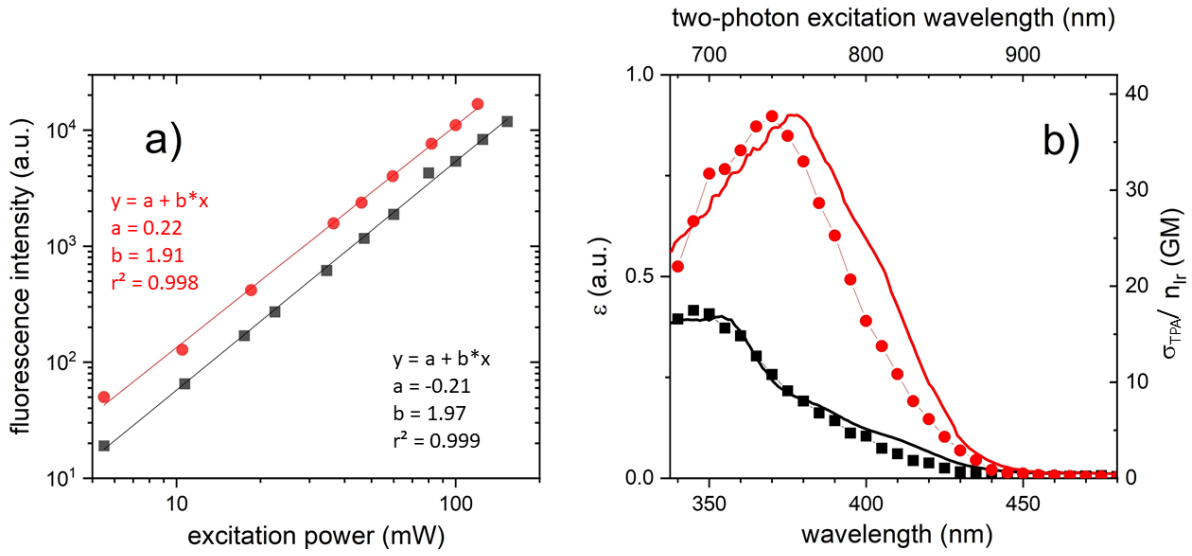

Figure 3 : (a) The luminescence intensity as a function of the excitation power at 800 nm, (b) two-photons (symbols) absorption spectra normalized per Ir-centers (n_{Ir}) along with the arbitrarily normalized one-absorption spectra (solid) for IrL^1 (black) and Ir$_2$L^2 (red). The two-photon absorption spectra were measured at 40 mW excitation power.

Singlet oxygen generation

As mentioned above, the phosphorescence of both complexes is highly sensitive to molecular oxygen, indeed, as triplet energy of the emissive excited state is higher than 0.97 eV (~1270 nm), which corresponds to the energy difference of the triplet oxygen ground state and its lowest singlet excited state. In short, there is a competition between the relaxation of the triplet excited state of the PS and the Dexter energy transfer to the ground state oxygen generating $^1O_2$. The singlet oxygen generation quantum yields of both complexes were measured by the relative method in aerated $CHCl_3$ solution with phenalenone as standard using the Stern-Volmer plot for analysis (figure S8). **IrL^1**

and **Ir_2L^2** can generate singlet oxygen with high yields ϕ_Δ = 0.66 and 0.78, respectively. In view of the molecular singlet oxygen generation efficiency coefficient (ς_Δ),[21,22] the bimetallic **Ir_2L^2** complex which exhibits both the highest ϕ_Δ and ε_{420nm} values, proves to be a more effective PS than **IrL^1**, nearly five times greater ς_Δ than **IrL^1**. In addition, **Ir_2L^2** displays a higher *figure of merit* at 780 nm than its monometallic counterpart.

The voltammetry cyclic was performed in acetonitrile using Bu_4NPF_6 (0.1 M) as the supporting electrolyte against Ag^+/Ag (ANE2, Table 1 and Table S1).[46] The redox potentials of **IrL^1** and **Ir_2L^2** are almost identical, differing by only 10 mV both in reduction and oxidation. The one e^- potential reduction of O_2 to $O_2^{\bullet-}$ is -0.33 V *vs* SHE and considering the excited state potentials *vs* SHE (Table S1) of **IrL^1** (E^{red}* = 1.34 V and E^{ox}* = 0.87 V) and **Ir_2L^2** (E^{ox}* = -0.84 V and E^{red}* = 1.33 V), it comes out that the complexes could be able to proceed to the reduction of ground state oxygen (Figure S9) leading to superoxide radical ion $O_2^{\bullet-}$. However, the complexes demonstrate high ϕ_Δ which is in contradiction. Indeed, the energy transfer to $^3O_2$ to produce $^1O_2$ competes kinetically with the single electron transfer reaction and the letter is less likely because of the biradical nature of ground state oxygen.[64] That being said, the electron transfer is favored in polar solvent and the presence of $O_2^{\bullet-}$ could be considered in the cells, in addition of $^1O_2$.[64] The electron transfer could be assessed by electron paramagnetic resonance spectroscopy (EPR) using 5,5-dimethyl-1-pyrroline N-oxide (DMPO), a known for trapping $O_2^{\cdot-}$ upon light illumiation.[65] Unfortunately, we were unable to observed the EPR signal corresponding the DMPO radical despite our attempts.

To conclude on the photophysical properties of the two complexes, our results clearly demonstrate that the binuclear complex, **Ir_2L^2**, is highly promising for imaging applications, exhibiting a brightness four times greater than that of the mononuclear complex, **IrL^1**, with B values of 13.3 x 10^3 and 3 x 10^3, respectively. Considering the two-photon absorption, once again **Ir_2L^2** displays better properties compared to **IrL^1,** with an enhancement in the two-photon absorption cross section maximum, σ_{TPA} = 18 G.M at 700 nm, σ_{TPA} 80 G.M. at 740 nm, for **IrL^1** and **Ir_2L^2** respectively. Finally, the ability of the complexes to sensitize oxygen for singlet oxygen generation confirms that **Ir_2L^2** is a significantly more effective photosensitizer than **IrL^1**, especially when considering the ς_Δ coefficient and the *figure of merit* parameters. With these results in hand, we decided to undertake *in vitro* studies to evaluate both complexes as PS in PDT.

Cellular uptake

The cellular uptake of **IrL^1** and **Ir_2L^2** was first evaluated in two different human cancer cell lines and was found to be slower for **Ir_2L^2** than for **IrL^1**. Indeed, confocal microscopy showed that both **IrL^1** and **Ir_2L^2** were mostly found in the cytoplasm of A549 (Figure 4A and 4B) and HT29 cells (Figure S10), confirming their internalization. **IrL^1** showed a diffuse labelling from 2 to 24 h incubation at 37 C. In contrast, **Ir_2L^2** showed a punctate labelling that increased over time, which is a hallmark of its intracytoplasmic trafficking after internalization. These results were confirmed by flow cytometry analyses: peak and mean fluorescence intensities were high for **IrL^1** and similar after 4h or 24h, while they were higher for **Ir_2L^2** after 24h than after 4h (Figure 4C and 4D). These differences between **IrL^1** and **Ir_2L^2** staining suggested that the **IrL^1** may enter cells by passive diffusion, whereas **Ir_2L^2** may use an active internalization process. However, internalization of both **IrL^1** and **Ir_2L^2** was prevented at 4°C (Figure 4C, 4D, and S11), suggesting that both **IrL^1** and **Ir_2L^2** entered cells through active internalization processes. Colocalization experiments with organelle-specific fluorescent dyes showed that the red fluorescent signal of **IrL^1** strongly overlapped that corresponding to the mitochondria (Figure 4E). In contrast, the red fluorescent signal of **Ir_2L^2** did not colocalize with either lysosomes or mitochondria (Figure 4E). These results indicate that **IrL^1** accumulates in mitochondria, as expected with most Iridium(III) complexes,[66] while **Ir_2L^2** may be retained in the cytosol or another organelle.

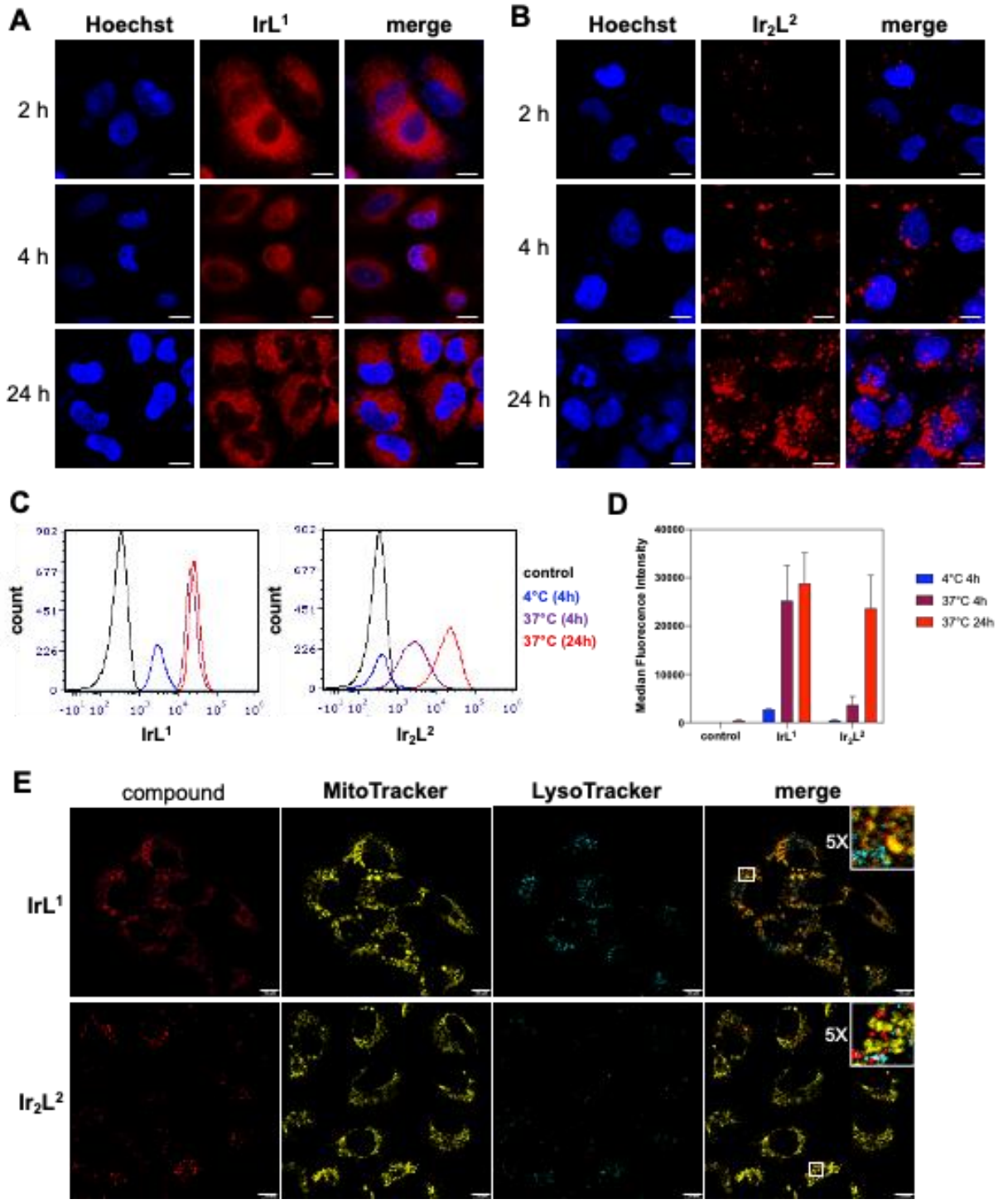

Figure 4 : IrL^1 and Ir_2L^2 are internalized in A549 cells. (A-B) Representatives confocal microscopy images of A549 cells incubated with 1 µmol.L^{-1} IrL^1 (A) or Ir2L2 (B) for 2 h, 4 h or 24 h. Nuclei are stained with Hoechst 33342 (in blue). IrL^1 and Ir_2L^2 fluorescence is observed in red. Scale bars, 10 µm. (C-D) Flow cytometry analysis (C) and corresponding quantitative results (D) of the cellular uptake of 1 µmol.L^{-1} IrL^1 or Ir_2L^2 after 4 h at 4°C or 37°C or after 24 h at 37°C. Data are expressed as mean ± standard deviation (n=2). (E) Colocalization of IrL^1 or Ir_2L^2 and organelle-specific probes in A549 cells. IrL^1 or Ir_2L^2 (red), MitoTracker orange (yellow), LysoTracker blue (cyan). Scale bars, 10 µm.

Phototoxicity in cells

We investigated the phototoxicity of **IrL^1** and **Ir$_2$L^2** *in vitro*. First, we assessed that illumination at 420 nm, in the absence of the compounds, induced only a moderate level of phototoxicity (Figure S12). Increasing concentrations of **IrL^1** and **Ir$_2$L^2** exposed to light reduced the viability of A549 and HT29 cells, whereas they had less toxic effect on the proliferation in the dark (Figure S13). Both A549 and HT29 cells appeared to be equally highly sensitive to **IrL^1** treatments, with similar IC_{50} values in the nanomolar range (Table 2 and Figure S13 and S14). In contrast, A549 and HT29 cells were less sensitive to **Ir$_2$L^2** treatments, with IC_{50} values in the range of several hundred nanomolar (Table 2 and Figure S13 and S15).

Table 2 : Sensitivity of cancer cells to IrL^1 and Ir$_2$L^2

Cell lines	Treatment conditions		IrL^1 IC_{50} (nmol L^{-1})	Ir$_2$L^2 IC_{50} (µmol L^{-1})
A549	4h	Dark	490 ± 30	5.12 ± 0.49
		10 J cm^{-2}	27 ± 3	2.22 ± 0.29
		25 J cm^{-2}	3 ± 1	0.23 ± 0.03
	24h	Dark	164 ± 11	3.17 ± 0.29
		10 J cm^{-2}	25 ± 0	0.66 ± 0.04
		25 J cm^{-2}	6 ± 1	0.29 ± 0.01
HT29	4h	Dark	356 ± 37	6.76 ± 0.50
		10 J cm^{-2}	34 ± 2	4.15 ± 0.28
		25 J cm^{-2}	15 ± 1	1.85 ± 0.12
	24h	Dark	229 ± 18	5.41 ± 0.45
		10 J cm^{-2}	14 ± 1	0.91 ± 0.05
		25 J cm^{-2}	7 ± 1	0.50 ± 0.03

The drug concentrations required to inhibit cell growth by 50% (IC50) at 4 h or 24 h in A549 or HT29 cells after light exposure (420 nm; 10 and 25 J cm-2). Data represent the mean ± SEM of 3 independent experiments, each performed in triplicate.

Interestingly, the phototoxicity of **IrL^1** and **Ir$_2$L^2** was light-dose dependent (Figure 5A, 5B and Figure S13). Furthermore, in agreement with our cellular uptake experiments, the 4 h drug-light interval (exposure to light 4 h after treatment) allowed **IrL^1** to induce the same high phototoxicity in A549 and HT29 cancer cells in vitro (Figure 5A) than the 24 h drug-light interval (Figure S14). In contrast, **Ir$_2$L^2** required a 24 h drug-light interval to induce significant phototoxicity (Figure 5B) as compared with the 4 h drug-light interval, especially in HT29 cells (Figure S15).

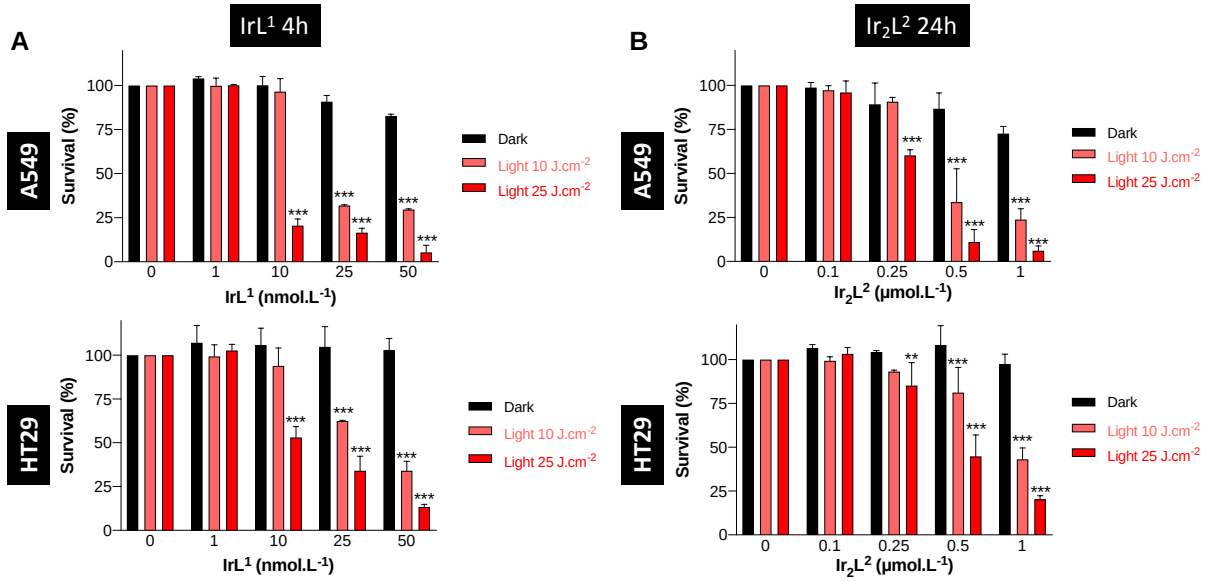

Figure 5 : IrL^1 and Ir_2L^2 induced phototoxicity in A549 and HT29 cells. A549 cells (upper panels) and HT29 cells (lower panels) were treated with increasing concentrations of IrL^1 for 4 h (A) or Ir2L2 for 24 h (B) before light exposure at 420 nm (fluency 10 J.cm-2 and 25 J.cm-2). In parallel, cells were maintained in the dark. Cell viability was assessed 72 h following light exposure. Data are expressed as the mean ± SD of 3 independent experiments in triplicate. ** p < 0.01; *** p < 0.001; significantly different from the Dark; ANOVA with Dunnett's post hoc tests.

A similar complex to **IrL^1** featuring a 2-(pyridinyl)-1-H-benzimidazole ancillary ligand instead of the ligand 1-butyl-5-methyl-2-(pyridinyl)-1-H-benzimidazole, displays lower dark toxicity on both A549 and HeLa.[67] In addition, with an almost identical fluence of irradiation at 425 nm (LED light array with 1.2 J cm^{-2}, 4 mW cm^{-2}, 300 s); the compound displays a phototoxicity of 1.39 ± 0.05 µM and 0.95 ± 0.04 µM for HeLa and A549, respectively, which are lower than those observed with **IrL^1**. Other dinuclear Ir complexes studied as molecular PS displayed similar phototoxicity properties in the µmol range than **Ir_2L^2**.[40,44] A shared properties could be the relative long incubation time for this type of complexes, at least 12h.

ROS generation in cells

We next assessed the generation of intracellular reactive oxygen species (ROS) by **IrL^1** and **Ir_2L^2** in A549 cells using the widely adopted nonspecific ROS probe, 2',7'-dichlorofluorescein diacetate (DCFH-DA). As shown in Figure 6A, following incubation with **IrL^1** and **Ir_2L^2**, A549 cells displayed green fluorescence signal when exposed to light (420 nm), especially after light dose of 10 J cm^{-2}, whereas only weak green fluorescence signal was observed in the control cells. The cellular fluorescence signal of DCFH-DA is strongly enhanced after illumination (Figure 6B). Cellular ROS production increased with **Ir_2L^2** concentration in a dose-dependent manner, while **IrL^1** induced high intracellular ROS production from the lowest concentrations studied.

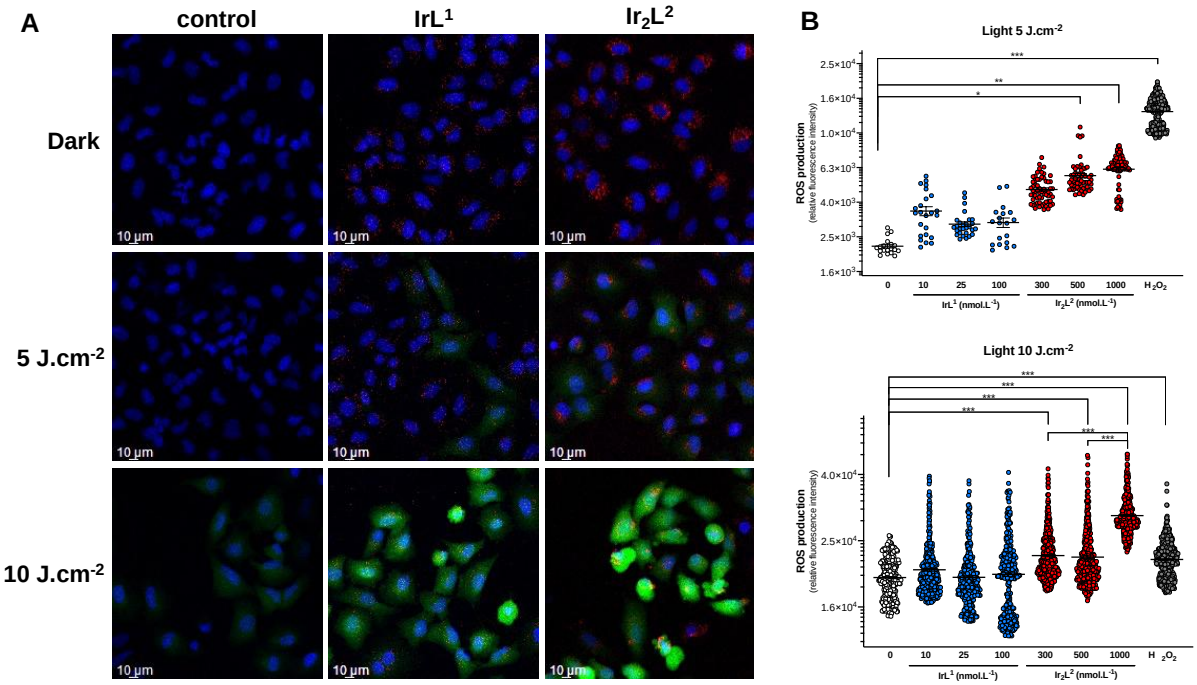

Figure 6 : IrL^1 and Ir_2L^2 generate cellular ROS in A549 cells after light exposure. (A) Confocal images of A549 cells incubated with 100 nmol.L^{-1} IrL^1 or 1 µmol.L^{-1} Ir_2L^2 (in red) for 24 h before light exposure at 420 nm (fluency 5 J.cm^{-2} and 10 J.cm^{-2}) and intracellular ROS detection by DCFH-DA (in green). Nuclei are stained with Hoechst 33342 (in blue). Scale bar = 10 µm. Images are representatives of 2 independent experiments. (B) ROS production in A549 cells treated with increasing concentrations of IrL^1 or Ir_2L^2 and 5 or 10 J.cm^{-2} light exposure at 420 nm. Bars: mean ± SEM (n=2). 100 µmol/L^{-1} hydrogen peroxide is used as positive control.

A similar phenomenon was observed with 800 nm fs laser irradiation. After incubation with **IrL^1** and **Ir_2L^2**, A549 cells showed a DCFH-DA green fluorescence signal in the area exposed to laser light, whereas only a weak green fluorescence signal was observed in control cells (Figure 7A). The fluorescence signal of DCFH-DA strongly increased after two-photon illumination, at the same time as the fluorescence of the compounds decreased particularly for **Ir_2L^2**. This ability to generate ROS suggested that **IrL^1** and **Ir_2L^2** could induce cell death after two-photon excitation. The complexes display a slight bleaching upon TPA illumination in cells, **Ir_2L^2** being the most impacted. The in vitro PDT efficacy of **IrL^1** and **Ir_2L^2** with two-photon irradiation was then assessed. Interestingly, cell morphological changes were observed a few hours after two-photon irradiation. As shown in Figure 7B, before laser illumination, A549 cells were well adhered with normal morphological characteristics. However, after illumination with 800 nm fs laser, the cells were rounded or detached, darkened, and with blebbing, all typical morphological features of cell death. By using live/dead staining, in which green calcein-AM and red propidium iodide (PI) stained live and dead cells, respectively, we showed that **IrL^1** and **Ir_2L^2** combined with 800 nm fs light irradiation efficiently killed A549 cells in the irradiation area (Figure 7B). Laser irradiation alone did not induce cell death. These results suggested that **IrL^1** and **Ir_2L^2** could be effective PS for TPE PDT.

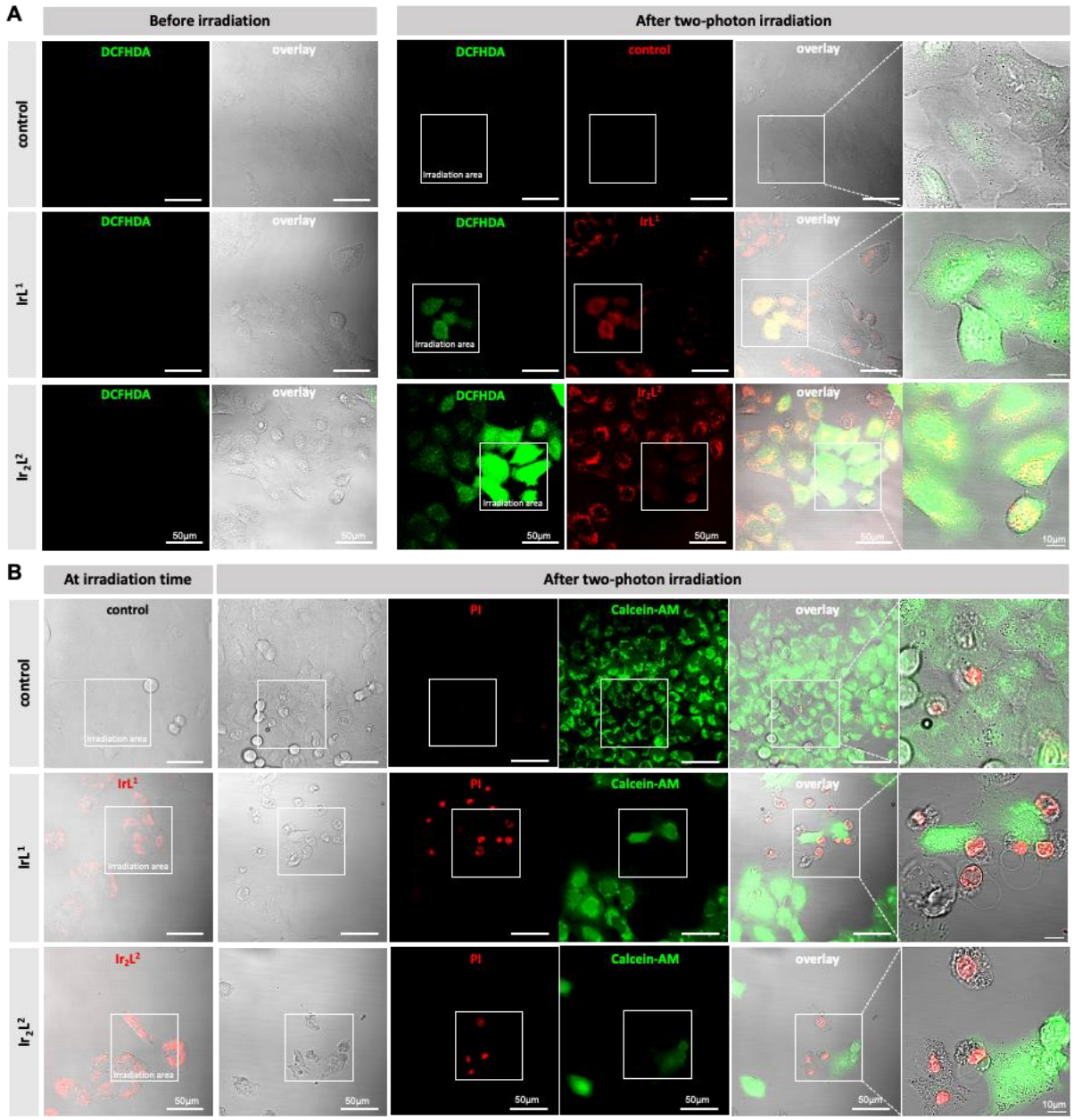

Figure 7: IrL¹ and Ir₂L² generate cellular ROS and cell death in A549 cells after two-photon irradiation. (A) Generation of intracellular ROS as detected by DCFH-DA (in green) in A549 cells incubated with or without IrL¹ or Ir₂L² (in red) for 24 h before and following irradiation of a square with 800 nm fs laser for 2 min. (B) Confocal microscopy images showing A549 cells incubated with or without IrL¹ or Ir₂L² (in red) at irradiation time and cell viability using calcein-AM (in green) and propidium iodide (in red) 15 h after *following irradiation of a square with 800 nm fs laser for 2 min. Scale bars, 50 μm and 10 μm in zoom sections.*

Conclusion

We report two Ir(III) complexes for PDT applications, a monomer (**IrL¹**) and a dimer (**Ir₂L²**). These complexes have been fully characterized and display phosphorescent emission in the orange-red region of the visible spectrum with high photoluminescence quantum yields. The spectroscopic investigations allow to attribute the emission to the radiative deactivation of the ^{3}MLCT excited state to the ground state. Both complexes can generate $^1O_2$ in good quantum yield, especially **Ir₂L²** of which ϕ_Δ is nearly 80%. The TPE spectra have been determined for both complexes and the σ_{TPA} maximum is dramatically increased for the dimer and has a concomitant bathochromic shift, which is also observed in absorption. Thus, we believe that our results may have an impact in the design of a new

generation of Ir(III) complexes for TPE. Indeed, considering both the molecular $^1O_2$ generation efficiency coefficient ζ_Δ and the *figure of merit* highlight the advantageous properties of **Ir_2L^2**, which dramatically surpasses **IrL^1**. However, this advantage is not observed in cells, which internalize **Ir_2L^2** more slowly than **IrL^1**. The latter displays high phototoxicity, with IC_{50} of 27-34 nmol after 4h of incubation and low illumination power for both cell lines. In addition, TPE appears to generate ROS and cell death with both **IrL^1** and **Ir_2L^2**. Our results put in light the advantages of designing multinuclear metal complexes for PDT applications by a molecular approach and may be used as guidelines in the field. Further work is still needed on the cell delivery aspects to take full advantage of the multimetallic's photophysical properties.

Experimental details: general consideration

Synthesis: Commercially available reagents were purchased from Sigma-Aldrich, Alfa Aesar, Acros Organics, TCI Chemical, Merck, Strem, Fluorochem, or bldpharma and used as received unless otherwise specified. Solvents were obtained from the same commercial sources and used without further purification. For moisture sensitive reactions, glassware was oven-dried prior to use. ^{1}H NMR spectra were recorded on a 400 MHz and on a 500 MHz in deuterated solvent ($CDCl_3$, DMSO-d_6 or CD_2Cl_2) and data are reported as follows: chemical shift in ppm from tetramethylsilane with the solvent as an internal indicator ($CDCl_3$ 7.26 ppm, CD_2Cl_2 5.32 ppm), multiplicity (s = singlet, d = doublet, t = triplet, q = quartet, p = pentet, hept = heptuplet, m = multiplet or overlap of non-equivalent resonances), J-coupling constants (Hz), and proton integration. $^{13}C\{^1H\}$ NMR spectra were recorded either at 101 MHz or at 126 MHz in suitable deuterated solvent and data are reported as follows: chemical shift in ppm from tetramethylsilane with the solvent as an internal indicator ($CDCl_3$ 77.16 ppm, DMSO-d_6 39.52 ppm, CD_2Cl_2 53.84 ppm. The ligands, L^1 and L^2, and the complexes, IrL^1 and Ir_2L^2, were synthetized according to our reported procedure.[46]

Electrochemistry: Cyclic voltammograms were recorded with a BioLogic SP-300 potentiostat. All electrochemical measurements were performed in a standard three-compartment electrochemical cell under an argon atmosphere using tetra-n-butylammonium hexafluorophosphate ($TBAPF_6$, Aldrich) as supporting electrolyte (0.1 M) in dry CH_3CN. Silver/silver nitrate in CH_3CN ($Ag/AgNO_3$ 10 mM in CH_3CN, ANE2) was used as reference, counter electrodes was a Pt wire, and the working electrode a 3 mm diameter glassy carbon disk.

Absorption and emission spectroscopies: Absorption spectra were recorded on a Cary 300 UV−visible spectrophotometer (Varian) and emission spectra (in solution at room temperature and in rigid matrix at 77 K) were recorded on a Horiba Fluoromax 4 or on FLS-1000 Edinburgh Instrument equipped with a photomultiplier (PMT) detector cooled by a Peltier. Quartz cuvettes with 1 cm optical path were used. Lifetimes were measured using LP900 spectrometer with a Flashlamp pumped by Q-switched Nd:Yag laser operating at 355 nm and with a photomultiplier (PMT) detector, or with a picosecond laser diode operating at 405 nm and using a time-correlated single photon counting detection (TCSPC, PicoHarp 300). Singlet oxygen emission was recorded using FLS-1000 Edinburgh Instrument equipped with a InGaAs detector, with quartz cuvettes with 1 cm optical path were used.

Emission quantum yields in solution were determined in deaerated CH_2Cl_2 solution at room temperature and calculated with the following equation.

$$QY_s = QY_{ref} \, X \, \frac{I_s}{I_{ref}} X \frac{A_{ref}}{A_s} X \left(\frac{\eta_s}{\eta_{ref}}\right)^2$$

QY_s corresponds to the quantum yield of the sample to be analysed, QY_{ref} is the quantum yield of the reference compound (in this work is $Ru(bpy)_3^{2+}$ in air equilibrated CH_3CN solution with value of 0.018±0.002)[68], I corresponds to the intensity of the emission (area of the spectrum), A is the absorption at the excitation wavelength, η corresponds to the refractive index of the solvents.

The two properties that provide information about the excited state beside the shape of the emission are the QY (Φ) and lifetime (τ), represented in the following equations.

$$\Phi = \frac{k_r}{k_r + k_{nr}} \quad \tau = \frac{1}{k_r + k_{nr}}$$

The radiative (k_r) and non-radiative (k_{nr}) constants can be obtained from combination and rearrangement of the QY (Φ) and τ equations to give equations:

$$k_r = \frac{\Phi}{\tau} \qquad k_{nr} = \frac{1}{\tau} - k_r$$

Singlet oxygen generation yields in solution were determined using the Stern-Vollmer equation in deaerated CH_3Cl solution at room temperature and calculated with the following equation.

$$f\Delta_x = f_{\Delta ST} \, X \, \frac{Grad x}{Grad_{ST}} X \left(\frac{\eta_s}{\eta_{ref}}\right)^2$$

$\phi_{\Delta x}$ corresponds to the singlet oxygen generation quantum yield of the sample to be analysed, $\phi_{\Delta\ ST}$ is the singlet oxygen generation quantum yield of the standard compound (in this work is phenalenone in air equilibrated CH_3Cl solution with value of 0.98), Grad the gradient from the plot of integrated fluorescence intensity vs absorbance **η** corresponds to the refractive index of the solvents.

Two-photon experiments

The two-photons absorption cross-sections, σ_{TPA} of **IrL^1** and **Ir$_2$L^2** were measured by the two-photons excited fluorescence (TPEF) technique. This method consists of measuring the two-photons absorption induced emission and comparing it to that of reference compounds with known σ_{TPA}.[69] The TPEF experiments were performed using a home-made setup. The excitation source was a tunable, femtosecond Ti-sapphire laser (Chameleon Ultra II, Coherent, 80 MHz), which was focused on a quartz spectroscopic cell containing the sample. The emitted light was collected at right-angle relative to the excitation beam and after removal of the scattered laser light with a low-pass filter, it was coupled to an optical fiber connected to CCD-spectrometer. The cell position was adjusted to reduce the optical path length of the exciting and emitted light in the cell reducing absorption by the solvent and inner-filter effect respectively.

The samples were dissolved in dichloromethane and continuously stirred during the experiment to avoid eventual photodegradation. The measurements were performed in aerated conditions.

The two-photons cross section was evaluated at several excitation wavelengths by tuning the excitation laser. The measured luminescence spectra were spectrally corrected. The two-photons cross section values were calculated in comparison to a reference compound as follows:

$$\sigma_{TPA,X} = \sigma_R \frac{\phi_R \cdot P^2{}_R \cdot c_R \cdot A_X \cdot I_X^m}{\phi_X \cdot P^2{}_X \cdot c_X \cdot A_R \cdot I_R^m}, \qquad (1)$$

where I^m corresponds to the maximum of the luminescence intensity, A is the normalized and integrated fluorescence spectrum, ϕ corresponds to the fluorescence quantum yield, c is the fluorophore concentration and P is the incident average laser power. The indices X and R denote the unknown and reference compounds respectively. Fluorescein ($5x10^{-5}$ mol·L^{-1}) dissolved in deuterated water at pH 13 was used as a two-photons absorption cross-section reference.[70]

Synthesis of the complexes IrL^1 and Ir_2L^2:[46]

General procedure: [μ-Cl_2(Ir(ppy)$_2$)][46] (ppy = 2-phenylpyridine) was suspended in a mixture of CH_2Cl_2/MeOH (1:1) and the ligand (2 eq. in the case of **IrL^1** and 1-0.9 eq. for **Ir_2L^2** was added. The yellow solution became rapidly orange after a few minutes and the reaction was refluxed overnight under Ar. At r.t., the solvent was concentrated to the 1/3rd, an excess of aqueous KPF_6 (sat.) was added drop-by-drop and an orange precipitate appeared rapidly, and the suspension was stirred an additional 10 min. The solution was filtrated off with a millipor® apparatus. The solid was washed with water, ice-cold methanol (5 mL) and finally with ice cold diethylether. The reaction gave clean complexes which were isolated as a dark yellowish to orange-red solid.

IrL^1: [μ-Cl_2(Ir(ppy)$_2$)] (50 mg, 0.05 mmol) was suspended in a mixture of CH_2Cl_2/MeOH (10 mL, 1:1) and the ligand **L^1** (32 mg, 0.09 mmol) was added. The refluxing yellow solution became rapidly orange after few minutes and the reaction was stirred overnight under Ar. At r.t., the solvent was concentrated to the 1/3rd, an excess of aqueous KPF_6 (sat.) was added drop-by-drop and an orange precipitate appeared rapidly, and the suspension was stirred an additional 10 min. The solution was filtrated off with a Millipor® apparatus. The solid was washed with water (10 mL), ice-cold methanol (5 mL) and finally with ice cold diethylether (15 mL). **IrL^1** was obtained pure after recrystallization by vapor diffusion of diethylether to a concentrated CH_2Cl_2 solution as a yellow powder. (87 mg, 93%). ^{1}H NMR (500 MHz, $CDCl_3$) δ 8.34 (dd, J = 8.8 Hz, J = 2.2 Hz, 1H), 8.26 (d, J = 8.8 Hz, 1H), 8.06 (d, J = 2.1 Hz, 1H), 7.98 (d, J = 8.2 Hz, 1H), 7.89 (d, J = 8.4 Hz, 1H), 7.81 – 7.70 (m, 4H), 7.62 (dd, J = 5.7 Hz, J = 1.6 Hz, 1H), 7.52 (dd, J = 5.7 Hz, J = 1.8 Hz, 1H), 7.35 (s, 1H), 7.13-7.09 (m, J = 7.6 Hz, J = 4.5 Hz, 1.2 Hz, 2H), 7.05 – 6.91 (m, 4H), 6.89 (dd, J = 8.7 Hz, J = 1.5 Hz, 1H), 6.37 (dd, J = 7.7, 1.2 Hz, 1H), 6.33 (dd, J = 7.6 Hz, J = 1.2 Hz, 1H), 6.23 (d, J = 8.6 Hz, 1H), 4.81 – 4.67 (m, 2H), 2.45 (s, 3H), 2.03 – 1.90 (m, J = 6.7 Hz, 2H), 1.47 (h, J = 7.5 Hz, 2H), 0.99 (t, J = 7.3 Hz, 3H).^{13}C NMR (126 MHz, $CDCl_3$) δ 168.2, 168.1, 153.5, 151.0, 150.6, 149.8, 149.0, 146.8, 146.4, 144.5, 144.4, 142.8, 138.6, 138.3, 138.1, 138.0, 137.3, 132.2, 132.0, 131.3, 130.5, 128.0, 125.6, 125.5, 125.0, 124.7, 123.8, 123.6, 123.3, 123.0, 120.3, 119.8, 118.3, 111.4, 46.3, 32.2, 22.2, 20.4, 13.9.

Ir_2L^2: [μ-Cl_2(Ir(ppy)$_2$)] (50 mg, 47 mmol), ligand **L^2** (31 mg, 47 mmol) and solvent 10 mL. The **Ir_2L^2** mixture was isolated after recrystallisation by vapor diffusion of diethylether to a CH_2Cl_2 solution, as a dark yellowish solid (72 mg, 79%). ^{1}H NMR (400 MHz, $(CD_3)_2CO$) δ 8.76 (d, J = 8.7 Hz, 2H), 8.57 (d, J = 8.9 Hz, 3H), 8.28 (t, 1H J = 8.0 Hz), 8.21 (s, 1H), 8.16 (dd, J = 8.2 Hz, 2H), 8.10 – 8.03 (m, 3H), 8.02 – 7.93 (m, 8H), 7.90 (t, J = 7.7 Hz, 2H), 7.26 (dd, J = 7.4 Hz, 2H), 7.19 – 6.95 (m, 10H), 6.83 (d, J = 8.2 Hz, 3H), 6.52 (t, J = 6.0 Hz, 2H), 6.41 (d, J = 7.7 Hz, 2H), 5.10 (d, J = 5.1 Hz, 2H), 1.56-1.40 (m, 4H), 0.98 (t, J = 7.4 Hz, 6H). ^{13}C NMR (101 MHz, $(CD_3)_2CO$) δ 172.9, 172.7, 157.8, 157.5, 156.1, 155.3, 155.1, 155.0, 152.3, 151.4, 150.1, 149.6, 147.6, 145.3, 143.9, 143.6, 141.8, 141.5, 137.7, 136.8, 135.7, 135.1, 131.7, 130.7, 130.3, 130.0, 129.4, 128.8, 128.0, 127.8, 125.1, 124.7, 117.8, 51.1, 36.9, 24.8, 18.3.

Electrochemistry

Cyclic voltammograms were recorded with a BioLogic SP-300 potentiostat. All electrochemical measurements were performed in a standard three-compartment electrochemical cell under an argon atmosphere using tetra-n-butylammonium hexafluorophosphate (TBAPF6, Aldrich) as supporting electrolyte (0.1 M) in dry CH3CN. Silver/silver nitrate in CH3CN (Ag/AgNO3 10 mM in CH3CN, ANE2) was used as reference, counter electrodes was a Pt wire, and the working electrode a 3 mm diameter glassy carbon disk.

Cell Lines and culture

The human lung adenocarcinoma A549 and colon carcinoma HT29 cell lines were obtained from LGC standard (Molsheim, France). All cells were routinely tested for the presence of mycoplasma (Mycoalert® Mycoplasma Detection Kit, Lonza, Rockland, ME, USA) and used within three months after thawing. Cells were maintained in culture at 37 °C in RPMI-1640 medium (A549) or in DMEM medium (HT29), with 10% FBS in a 5% CO2 humidified atmosphere. The cell morphology was routinely checked.

Cellular uptake

Cells were plated on labtek® and treated with 1 µmol.L^{-1} **IrL^1** or **Ir$_2$L^2** for 2 h, 4 h, or 24 h in the dark at 37 °C, or for 4 h at 4 °C, before confocal imaging. Hoechst (5 µmol.L^{-1}) was used to counterstain the cell nuclei. Fluorescence microscopy was carried out using a confocal microscope (LSM 710; Carl Zeiss, Jena, Germany). An objective Plan Apochromat 20×/0.8 NA in air and an objective Plan Apochromat 63×/1.4 NA in oil were used. The excitation was at 405 nm and emission filter between 600 and 760 nm for **IrL^1** and **Ir$_2$L^2**, and between 415 and 500 nm for Hoechst. The cells were also collected and quantified by flow cytometry (Attune NxT, Thermo Fisher Scientific, New York city, NY, US). Flow cytometric analysis was performed using FCS Express 7 software (De Novo Software, Dotmatics, Pasadena, CA, US).

Subcellular localization

Cells were plated on labtek® and treated with 1 µmol.L^{-1} **IrL^1** or **Ir$_2$L^2** for 24 h in the dark at 37 °C. The cells were then stained with 25 nmol.L^{-1} MitoTracker Orange and 120 nmol.L^{-1} LysoTracker blue (Invitrogen, ThermoFisher Scientific) for 30 min at 37°C. The cells were then washed with PBS to eliminate any excess dye and were immediately examined using a Stellaris confocal microscope. A 63x objective (HC PL APO CS2, 1.2 water) was used. The fluorescence images from dyes were collected in the range λ_{em} = 410-455 nm (λ_{exc} = 405 nm) for LysoTracker, and in the range λ_{em} = 556-642 nm (λ_{exc} = 551 nm) for MitoTracker. Both **IrL^1** and **Ir$_2$L^2** were imaged in the range λ_{em} = 670-800 nm (λ_{exc} = 405 nm).

Irradiation of the cells

Illumination at 420 nm with power output at 78.125 mW.cm^{-2} (1 min and 4 s, fluency 5 J.cm^{-}2; 2 min and 8 s, fluency 10 J.cm^{-2}; and 5 min and 20 s, fluency 25 J.cm^{-2}) was performed after treatment using Lumidox® II 96-position LED Array (Anaytical Sales and Services, Flanders, NJ, US). Two-photon illlumination was performed at λ= 800 nm with a Ti:Sapphire laser (Chameleon Vision II, Coherent, > 3 W, 140 fs pulses, 80MHz repetition rate).

ROS generation in cells

A549 cells were seeded overnight for adherence and then incubated with **IrL^1** and **Ir$_2$L^2** for 24 h. Twenty-five µmol.L^{-1} 2′,7′-dichlorofluorescein diacetate (H2DCFH-DA, Sigma-Aldrich, France) were then incubated for 30 min. Hoechst (5 µmol.L^{-1}) was used to counterstain the cell nuclei. The fluorescence images before and after 420 nm irradiation were acquired using a Stellaris 8 confocal microscope equipped with a white laser (Leica Microsystems). A 10x objective (HC PL APO, NA=0.40) was used to collect the light. The emission from the Hoechst dye was collected in the range λ_{em} = 412-464 nm (HyD detector), upon excitation with the 405 nm laser diode. Both photosensitizers were imaged using the same excitation diode (λ_{exc} = 405 nm) and the emission was collected within the range λ_{em} = 670-800 nm (HyD detector). The emission of the DCF dye was measured upon excitation at λ_{exc} = 491 nm and the light was collected in the range λ_{em} = 500-547 nm (HyD detector). Image analysis was conducted using the “Analysis” module within the LasX software of the Stellaris microscope. Each cell was individually identified and the mean intensity of emission of the DHF dye was quantified per cell. The fluorescence images before and after 800 nm irradiation were acquired using a confocal microscope (LSM 710, Zeiss) with a 40x/1.2 W Plan Apochromat objective.

In vitro cytotoxicity assays

Cell proliferation assays were conducted in 96-well culture plates. Cells were cultured for 24 h prior to treatment with increasing concentration of **IrL^1** or **Ir$_2$L^2** for in complete medium. Illumination at 420 nm was performed 4 h or 24 h after treatment. The cell viability was quantified 72 h after light exposure with the 3-(4,5-dimethylthiazol-2-yl)-2,5-diphenyltetrazolium bromide assay (MTT assay). Cell viability was normalized to control cells (no drug and un-illuminated). The drug concentrations required to inhibit cell growth by 50% (IC_{50}) were determined by interpolation from the dose to response curves.

For live/dead cell staining, A549 cells were incubated with **IrL^1** or **Ir$_2$L^2** for 24 h, irradiated at 800 nm, and stained with 2 µmol.L-1 calcein-AM (Invitrogen, ThermoFisher Scientific) and 3 µmol.L-1 PI (Sigma-Aldrish) after 15h.

ASSOCIATED CONTENT

Supporting Information is material is available free of charge via the Internet at http://pubs.acs.org. The reader will find synthesis scheme overviews, information about the Structural characterization, and the NMR spectra.

Author Contributions

The manuscript was written through contributions of all authors.

ACKNOWLEDGMENT

This work is supported by the French National Research Agency in the framework of the "Investissements d'avenir" program (ANR-15-IDEX-02). This work has been partially supported by CBH-EUR-GS (ANR-17-EURE-0003). The authors would like to thank Kamilla Mammadzada and Dr. Maria V. Vlasova who participated with enthusiasm to the project during their internships. The Nano-Bio ICMG (UAR 2607), is acknowledged for providing facilities for mass spectrometry (A. Durand, L. Fort and R. Gueret) and single crystal X-ray diffraction (N. Altounian). A-L.B. acknowledges the support of the European Research Council (ERC STG, RADIANCE, 101116304). We acknowledge the MicroCell facility (GIS IBiSA, ISdV, IAB), member of the national infrastructure France-BioImaging supported by the French National Research Agency (ANR-24-INBS-0005 FBI BIOGEN) for optical microscopy. Views and opinions expressed are however those of the authors only and do not necessarily reflect those of the European Union or the European Research Council Executive Agency. Neither the European Union nor the granting authority can be held responsible for them.

References

(1) Xu, S.; Bulin, A. L.; Hurbin, A.; Elleaume, H.; Coll, J. L.; Broekgaarden, M. Photodynamic Diagnosis and Therapy for Peritoneal Carcinomatosis: Emerging Perspectives. *Cancers (Basel)* **2020**, *12* (9), 1–25. https://doi.org/10.3390/cancers12092491.

(2) Caporale, C.; Massi, M. Cyclometalated Iridium(III) Complexes for Life Science. *Coord Chem Rev* **2018**, *363*, 71–91. https://doi.org/10.1016/j.ccr.2018.02.006.

(3) Shen, J.; Rees, T. W.; Ji, L.; Chao, H. Recent Advances in Ruthenium(II) and Iridium(III) Complexes Containing Nanosystems for Cancer Treatment and Bioimaging. *Coord Chem Rev* **2021**, *443*, 214016. https://doi.org/10.1016/j.ccr.2021.214016.

(4) McKenzie, L. K.; Bryant, H. E.; Weinstein, J. A. Transition Metal Complexes as Photosensitisers in One- and Two-Photon Photodynamic Therapy. *Coord Chem Rev* **2019**, *379*, 2–29. https://doi.org/10.1016/j.ccr.2018.03.020.

(5) Chen, J.; Fan, T.; Xie, Z.; Zeng, Q.; Xue, P.; Zheng, T.; Chen, Y.; Luo, X.; Zhang, H. Advances in Nanomaterials for Photodynamic Therapy Applications: Status and Challenges. *Biomaterials* **2020**, *237*. https://doi.org/10.1016/J.BIOMATERIALS.2020.119827.

(6) Kessel, D. Clinical Medicine Photodynamic Therapy: A Brief History. **2019**. https://doi.org/10.3390/jcm8101581.

(7) Agostinis, P.; Berg, K.; Cengel, K. A.; Foster, T. H.; Girotti, A. W.; Gollnick, S. O.; Hahn, S. M.; Hamblin, M. R.; Juzeniene, A.; Kessel, D.; Korbelik, M.; Moan, J.; Mroz, P.; Nowis, D.; Piette, J.; Wilson, B. C.; Golab, J. Photodynamic Therapy of Cancer: An Update. *CA Cancer J Clin* **2011**, *61* (4), 250–281. https://doi.org/https://doi.org/10.3322/caac.20114.

(8) Obaid, G.; Celli, J. P.; Broekgaarden, M.; Bulin, A.-L.; Uusimaa, P.; Pogue, B.; Hasan, T.; Huang, H.-C. Engineering Photodynamics for Treatment, Priming and Imaging. *Nature Reviews Bioengineering* **2024**, *2* (9), 752–769. https://doi.org/10.1038/s44222-024-00196-z.

(9) Basic Principles of Photodynamic Therapy. *J Porphyr Phthalocyanines* **2001**, *05* (02), 105-.

(10) Obana, A.; Gohto, Y.; Kaneda, K.; Nakajima, S.; Takemura, T.; Miki, T. Selective Occlusion of Choroidal Neovascularization by Photodynamic Therapy with a Water-Soluble Photosensitizer, ATX-S10. *Lasers Surg Med* **1999**, *24* (3), 209–222. https://doi.org/https://doi.org/10.1002/(SICI)1096-9101(1999)24:3<209::AID-LSM6>3.0.CO;2-L.

(11) Lan, M.; Zhao, S.; Liu, W.; Lee, C.-S. S.; Zhang, W.; Wang, P. Photosensitizers for Photodynamic Therapy. *Adv Healthc Mater* **2019**, *8* (13).

(12) McKenzie, L. K.; Sazanovich, I. V.; Baggaley, E.; Bonneau, M.; Guerchais, V.; Williams, J. A. G.; Weinstein, J. A.; Bryant, H. E. Metal Complexes for Two-Photon Photodynamic Therapy: A Cyclometallated Iridium Complex Induces Two-Photon Photosensitization of Cancer Cells under Near-IR Light. *Chemistry - A European Journal* **2017**, *23* (2), 234–238. https://doi.org/10.1002/chem.201604792.

(13) Gunaydin, G.; Gedik, M. E.; Ayan, S. Photodynamic Therapy—Current Limitations and Novel Approaches. *Front Chem* **2021**, *9* (June), 1–25. https://doi.org/10.3389/fchem.2021.691697.

(14) Sherlock, B.; Warren, S. C.; Alexandrov, Y.; Yu, F.; Stone, J.; Knight, J.; Neil, M. A. A.; Paterson, C.; French, P. M. W.; Dunsby, C. In Vivo Multiphoton Microscopy Using a Handheld Scanner with Lateral and Axial Motion Compensation. *J Biophotonics* **2018**, *11* (2). https://doi.org/10.1002/jbio.201700131.

(15) Ho, P. Y.; Lee, S. Y.; Kam, C.; Zhu, J.; Shan, G. G.; Hong, Y.; Wong, W. Y.; Chen, S. Fluorescence Imaging and Photodynamic Inactivation of Bacteria Based on Cationic Cyclometalated Iridium(III) Complexes with Aggregation-Induced Emission Properties. *Adv Healthc Mater* **2021**, *2100706*, 1–9. https://doi.org/10.1002/adhm.202100706.

(16) Abad-Montero, D.; Gandioso, A.; Izquierdo-García, E.; Chumillas, S.; Rovira, A.; Bosch, M.; Jordà-Redondo, M.; Castaño, D.; Bonelli, J.; Novikov, V. V.; Deyà, A.; Hernández, J. L.; Galino, J.; Alberto, M. E.; Francés-Monerris, A.; Nonell, S.; Gasser, G.; Marchán, V. Ruthenium(II)

Polypyridyl Complexes Containing COUBPY Ligands as Potent Photosensitizers for the Efficient Phototherapy of Hypoxic Tumors. *J Am Chem Soc* **2025**, No. Ii. https://doi.org/10.1021/jacs.4c15036.

(17) Zhao, Q.; Huang, C.; Li, F. Phosphorescent Heavy-Metal Complexes for Bioimaging. *Chem Soc Rev* **2011**, *40* (5), 2508–2524.

(18) Dolmans, D. E. J. G. J.; Fukumura, D.; Jain, R. K. Photodynamic Therapy for Cancer. *Nat Rev Cancer* **2003**, *3* (5), 380–387.

(19) Bin Mohd Yusoff, Abd. R.; Huckaba, A. J.; Nazeeruddin, M. K. Phosphorescent Neutral Iridium (III) Complexes for Organic Light-Emitting Diodes. *Top Curr Chem* **2017**, *375* (2), 39. https://doi.org/10.1007/s41061-017-0126-7.

(20) Wu, S.; Galán, L. A.; Roux, M.; Riobé, F.; Guennic, B. Le; Bahers, T. Le; Micouin, L.; Maury, O.; Benedetti, E. Tuning the Excited State Properties of [2.2] Paracyclophane-Based Antennas to Ensure Efficient Sensitization of Lanthanide Ions or Singlet Oxygen Generation . *Inorg Chem* **2021**, *60* (21), 16194–16203. https://doi.org/10.1021/acs.inorgchem.1c01986.

(21) Ziani, Z. Exploitation de La Plateforme Moléculaire Diméthyldihydropyrène Pour Le Photochromisme , La Production et Le Stockage de Dioxygène Singulet . Corrélations Photostructurales, Univ. Grenoble Alpes PhD Thesis, Univ. Grenoble Alpes, 2023.

(22) Klausen, M.; Blanchard-Desce, M. Two-Photon Uncaging of Bioactive Compounds: Starter Guide to an Efficient IR Light Switch. *Journal of Photochemistry and Photobiology C: Photochemistry Reviews* **2021**, *48* (May), 100423. https://doi.org/10.1016/j.jphotochemrev.2021.100423.

(23) Prieto-Castaneda, A.; Lérida-Viso, A.; Avellanaal-Zaballa, E.; Sola-Llano, R.; Banuelos, J.; Agarrabeitia, A. R.; Martínez-Manez, R.; Ortiz, M. J. Phosphorogenic Dipyrrinato-Iridium (III) Complexes as Photosensitizers for Photodynamic Therapy. *Dye and Pigments* **2022**, *197*, 109886.

(24) Yang, P.; Zhang, S.; Wang, K.; Qi, H. Synthesis of PH-Responsive Cyclometalated Iridium(III) Complex and Its Application in the Selective Killing of Cancerous Cells. *Dalton Transactions* **2021**, *50* (46), 17338–17345. https://doi.org/10.1039/d1dt03042f.

(25) Wu, Y.; Wu, J.; Wong, W. Y. A New Near-Infrared Phosphorescent Iridium(III) Complex Conjugated to a Xanthene Dye for Mitochondria-Targeted Photodynamic Therapy. *Biomater Sci* **2021**, *9* (14), 4843–4853. https://doi.org/10.1039/d1bm00128k.

(26) Ye, R. R.; Tan, C. P.; He, L.; Chen, M. H.; Ji, L. N.; Mao, Z. W. Cyclometalated Ir(III) Complexes as Targeted Theranostic Anticancer Therapeutics: Combining Hdac Inhibition with Photodynamic Therapy. *Chemical Communications* **2014**, *50* (75), 10945–10948. https://doi.org/10.1039/c4cc05215c.

(27) Zhao, J.; Ji, S.; Wu, W.; Wu, W.; Guo, H.; Sun, J.; Sun, H.; Liu, Y.; Li, Q.; Huang, L. Transition Metal Complexes with Strong Absorption of Visible Light and Long-Lived Triplet Excited States: From Molecular Design to Applications. *RSC Adv 2* (5), 1712–1728. https://doi.org/10.1039/c1ra00665g.

(28) Majumdar, P.; Yuan, X.; Li, S.; Le Guennic, B.; Ma, J.; Zhang, C.; Jacquemin, D.; Zhao, J. Cyclometalated Ir(III) Complexes with Styryl-BODIPY Ligands Showing near IR

Absorption/Emission: Preparation, Study of Photophysical Properties and Application as Photodynamic/Luminescence Imaging Materials. *J Mater Chem B* **2014**, *2* (19), 2838–2854. https://doi.org/10.1039/c4tb00284a.

(29) Mizukami, K.; Katano, A.; Shiozaki, S.; Yoshihara, T.; Goda, N.; Tobita, S. In Vivo O2 Imaging in Hepatic Tissues by Phosphorescence Lifetime Imaging Microscopy Using Ir(III) Complexes as Intracellular Probes. *Sci Rep* **2020**, *10* (1), 1–14. https://doi.org/10.1038/s41598-020-76878-6.

(30) Novohradsky, V.; Rovira, A.; Hally, C.; Galindo, A.; Vigueras, G.; Gandioso, A.; Svitelova, M.; Bresolí-Obach, R.; Kostrhunova, H.; Markova, L.; Kasparkova, J.; Nonell, S.; Ruiz, J.; Brabec, V.; Marchán, V. Towards Novel Photodynamic Anticancer Agents Generating Superoxide Anion Radicals: A Cyclometalated IrIII Complex Conjugated to a Far-Red Emitting Coumarin. *Angewandte Chemie - International Edition* **2019**, *58* (19), 6311–6315. https://doi.org/10.1002/anie.201901268.

(31) Cai, X.; Wang, K. N.; Ma, W.; Yang, Y.; Chen, G.; Fu, H.; Cui, C.; Yu, Z.; Wang, X. Multifunctional AIE Iridium(III) Photosensitizer Nanoparticles for Two-Photon-Activated Imaging and Mitochondria Targeting Photodynamic Therapy. *J Nanobiotechnology* **2021**, *19* (1), 1–13. https://doi.org/10.1186/s12951-021-01001-4.

(32) Xu, Y.; Wang, X.; Song, K.; Du, J.; Liu, J.; Miao, Y.; Li, Y. BSA-Encapsulated Cyclometalated Iridium Complexes as Nano-Photosensitizers for Photodynamic Therapy of Tumor Cells. *RSC Adv* **2021**, *11* (25), 15323–15331. https://doi.org/10.1039/d1ra01740c.

(33) Liu, Y.; Zhu, D.; Xie, Z. Ir(III) Complex Dimer Nanoparticles for Photodynamic Therapy. *ACS Med Chem Lett* **2021**, *12* (9), 1374–1379. https://doi.org/10.1021/acsmedchemlett.1c00362.

(34) Li, L.; Zhang, L.; Tong, X.; Li, Y.; Yang, Z.; Zhu, D.; Su, Z.; Xie, Z. Near-Infrared-Emitting AIE Multinuclear Cationic Ir(III) Complex-Assembled Nanoparticles for Photodynamic Therapy. *Dalton Transactions* **2020**, *49* (43), 15332–15338. https://doi.org/10.1039/d0dt02962a.

(35) Yi, S.; Lu, Z.; Zhang, J.; Wang, J.; Xie, Z.; Hou, L. Amphiphilic Gemini Iridium(III) Complex as a Mitochondria-Targeted Theranostic Agent for Tumor Imaging and Photodynamic Therapy. *ACS Appl Mater Interfaces* **2019**, *11* (17), 15276–15289. https://doi.org/10.1021/acsami.9b01205.

(36) Denk, W.; Strickler, J. H.; Webb, W. W. Two-Photon Laser Scanning Fluorescence Microscopy. *Science (1979)* **1990**, *248*, 73–76. https://doi.org/10.1126/science.2321027.

(37) Strickler, J. H.; Webb, W. W. Three-Dimensional Optical Data Storage in Refractive Media by Two-Photon Point Excitation. *Optics Letter* **1991**, *16* (22), 1780–1782.

(38) McKenzie, L. K.; Bryant, H. E.; Weinstein, J. A. Transition Metal Complexes as Photosensitisers in One- and Two-Photon Photodynamic Therapy. *Coord Chem Rev* **2019**, *379*, 2–29. https://doi.org/10.1016/j.ccr.2018.03.020.

(39) Beverina, L.; Crippa, M.; Landenna, M.; Ruffo, R.; Salice, P.; Silvestri, F.; Versari, S.; Villa, A.; Ciaffoni, L.; Collini, E.; Ferrante, C.; Bradamante, S.; Mari, C. M.; Bozio, R.; Pagani, G. A. Assessment of Water-Soluble π-Extended Squaraines as One- and Two-Photon Singlet Oxygen Photosensitizers: Design, Synthesis, and Characterization. *J Am Chem Soc* **2008**, *130* (6), 1894–1902. https://doi.org/10.1021/ja075933a.

(40) Daniels, R. E.; McKenzie, L. K.; Shewring, J. R.; Weinstein, J. A.; Kozhevnikov, V. N.; Bryant, H. E. Pyridazine-Bridged Cationic Diiridium Complexes as Potential Dual-Mode Bioimaging Probes. *RSC Adv* **2018**, *8* (18), 9670–9676. https://doi.org/10.1039/c8ra00265g.

(41) Shafikov, M. Z.; Hodgson, C.; Gorski, A.; Kowalczyk, A.; Gapińska, M.; Kowalski, K.; Czerwieniec, R.; Kozhevnikov, V. N. Benzannulation of a Ditopic Ligand to Afford Mononuclear and Dinuclear Ir(Iii) Complexes with Intense Phosphorescence: Applications in Singlet Oxygen Generation and Bioimaging. *J Mater Chem C Mater* **2022**, *10* (5), 1870–1877. https://doi.org/10.1039/d1tc05271c.

(42) Congrave, D. G.; Hsu, Y.-T.; Batsanov, A. S.; Beeby, A.; Bryce, M. R. Sky-Blue Emitting Bridged Diiridium Complexes: Beneficial Effects of Intramolecular π–π Stacking. *Dalton Transactions* **2018**, *47* (47), 2086–2098. https://doi.org/10.1039/C7DT04201A.

(43) Li, G.; Congrave, D. G.; Zhu, D.; Su, Z.; Bryce, M. R. Recent Advances in Luminescent Dinuclear Iridium(III) Complexes and Their Application in Organic Electroluminescent Devices. *Polyhedron* **2018**, *140*, 146–157. https://doi.org/10.1016/j.poly.2017.11.029.

(44) Liu, B.; Monro, S.; Lystrom, L.; Cameron, C. G.; Colón, K.; Yin, H.; Kilina, S.; McFarland, S. A.; Sun, W. Photophysical and Photobiological Properties of Dinuclear Iridium(III) Bis-Tridentate Complexes. *Inorg Chem* **2018**, *57* (16), 9859–9872. https://doi.org/10.1021/acs.inorgchem.8b00789.

(45) Wang, Y.; Felder, P. S.; Mesdom, P.; Blacque, O.; Mindt, T. L.; Cariou, K.; Gasser, G. Towards Ruthenium(II)-Rhenium(I) Binuclear Complexes as Photosensitizers for Photodynamic Therapy. *ChemBioChem* **2023**, *n/a* (n/a), e202300467. https://doi.org/https://doi.org/10.1002/cbic.202300467.

(46) Lanoë, P.-H.; Philouze, C.; Vanthuyne, N.; Debsouri, K.; Crassous, J.; Loiseau, F. Phosphorescent Chiral Cationic Binuclear Iridium(III) Complexes: Boosting the CPL Brightness. *Inorg Chem* **2024**, *63*, 24855–24866.

(47) Murphy, L.; Congreve, A.; Pålsson, L. O.; Williams, J. A. G. The Time Domain in Co-Stained Cell Imaging: Time-Resolved Emission Imaging Microscopy Using a Protonatable Luminescent Iridium Complex. *Chemical Communications* **2010**, *46* (46), 8743–8745. https://doi.org/10.1039/c0cc03705b.

(48) Berezin, M. Y.; Achilefu, S. Fluorescence Lifetime Measurements and Biological Imaging. *Chem. Mater.* **2010**, *110* (5), 2641–2684. https://doi.org/10.1021/cr900343z.Fluorescence.

(49) Kelkar, S. S.; Reineke, T. M. Theranostics: Combining Imaging and Therapy. *Bioconjug Chem* **2011**, *22* (10), 1879–1903. https://doi.org/10.1021/bc200151q.

(50) Nagaya, T.; Nakamura, Y. A.; Choyke, P. L.; Kobayashi, H. Fluorescence-Guided Surgery. *Front Oncol* **2017**, *7* (DEC). https://doi.org/10.3389/fonc.2017.00314.

(51) Flamigni, L.; Barbieri, A.; Sabatini, C.; Ventura, B.; Barigelletti, F. Photochemistry and Photophysics of Coordination Compounds: Iridium. In *Photochemistry and Photophysics of Coordination Compounds II*; 2007; pp 143–203.

(52) Plummer, E. A.; Hofstraat, W.; Cola, L. De. Mono- and Di-Nuclear Iridium(III) Complexes. Synthesis and Photophysics. *Dalton Transactions* **2003**, 2080–2084.

(53) Culham, S.; Lanoë, P.-H.; Whittle, V. L.; Durrant, M. C.; Williams, J. A. G. A. G.; Kozhevnikov, V. N. Highly Luminescent Dinuclear Platinum(II) Complexes Incorporating Bis-Cyclometallating Pyrazine-Based Ligands: A Versatile Approach to Efficient Red Phosphors. *Inorg Chem* **2013**, *52* (19), 10992–11003. https://doi.org/10.1021/ic401131x.

(54) Lanoë, P.-H.; Tong, C. M.; Harrington, R. W.; Probert, M. R.; Clegg, W.; Williams, J. A. G.; Kozhevnikov, V. N. Ditopic Bis-Terdentate Cyclometallating Ligands and Their Highly Luminescent Dinuclear Iridium(III) Complexes. *Chemical communications* **2014**, *50* (52), 6831–6936. https://doi.org/10.1039/c4cc01808g.

(55) He, L.; Qiao, J.; Duan, L.; Dong, G.; Zhang, D.; Wang, L.; Qiu, Y. Toward Highly Efficient Solid-State White Light-Emitting Electrochemical Cells: Blue-Green to Red Emitting Cationic Iridium Complexes with Imidazole-Type Ancillary Ligands. *Adv Funct Mater* **2009**, *19* (18), 2950–2960. https://doi.org/10.1002/adfm.200900723.

(56) Sunesh, C. D.; Mathai, G.; Choe, Y. Constructive Effects of Long Alkyl Chains on the Electroluminescent Properties of Cationic Iridium Complex-Based Light-Emitting Electrochemical Cells. *ACS Appl Mater Interfaces* **2014**, *6* (20), 17416–17425. https://doi.org/10.1021/am5058426.

(57) Martínez-Alonso, M.; Cerdá, J.; Momblona, C.; Pertegás, A.; Junquera-Hernández, J. M.; Heras, A.; Rodríguez, A. M.; Espino, G.; Bolink, H.; Ortí, E. Highly Stable and Efficient Light-Emitting Electrochemical Cells Based on Cationic Iridium Complexes Bearing Arylazole Ancillary Ligands. *Inorg Chem* **2017**, *56* (17), 10298–10310. https://doi.org/10.1021/acs.inorgchem.7b01167.

(58) Turro, N. J.; Ramamurthy, V.; J. C. Scaiano. *Modern Molecular Photochemistry of Organic Molecules*; 2010.

(59) Wong, K. L.; Bünzli, J. C. G.; Tanner, P. A. Quantum Yield and Brightness. *J Lumin* **2020**, *224*, 117256. https://doi.org/10.1016/j.jlumin.2020.117256.

(60) Wu, C.; Bull, B.; Szymanski, C.; Christensen, K.; Mcneill, J. Multicolor Conjugated Polymer Dots for Biological Fluorescence Imaging. *ACS Nano* **2008**, *2* (11), 2415–2423. https://doi.org/10.1021/nn800590n.

(61) Lepeltier, M.; Appaix, F.; Liao, Y. Y.; Dumur, F.; Marrot, J.; Le Bahers, T.; Andraud, C.; Monnereau, C. Carbazole-Substituted Iridium Complex as a Solid State Emitter for Two-Photon Intravital Imaging. *Inorg Chem* **2016**, *55* (19), 9586–9595. https://doi.org/10.1021/acs.inorgchem.6b01253.

(62) Tian, X.; Zhu, Y.; Zhang, M.; Luo, L.; Wu, J.; Zhou, H.; Guan, L.; Battaglia, G.; Tian, Y. Localization Matters: A Nuclear Targeting Two-Photon Absorption Iridium Complex in Photodynamic Therapy. *Chemical Communications* **2017**, *53* (23), 3303–3306. https://doi.org/10.1039/c6cc09470h.

(63) Boreham, E. M.; Jones, L.; Swinburne, A. N.; Blanchard-Desce, M.; Hugues, V.; Terryn, C.; Miomandre, F.; Lemercier, G.; Natrajan, L. S. A Cyclometallated Fluorenyl Ir(III) Complex as a Potential Sensitiser for Two-Photon Excited Photodynamic Therapy (2PE-PDT). *Dalton Transactions* **2015**, *44* (36), 16127–16135. https://doi.org/10.1039/c5dt01855b.

(64) Bregnhøj, M.; Thorning, F.; Ogilby, P. R. Singlet Oxygen Photophysics: From Liquid Solvents to Mammalian Cells. *Chem Rev* **2024**, *124* (17), 9949–10051. https://doi.org/10.1021/acs.chemrev.4c00105.

(65) Liu, S.; Wang, Z.; Wu, Z.; Chen, H.; Zhu, D.; Li, G.; Yan, M.; Bryce, M. R.; Chang, Y. Long-Wavelength Triggered Iridium(Iii) Complex Nanoparticles for Photodynamic Therapy against Hypoxic Cancer. *Chemical Communications* **2024**, *5*. https://doi.org/10.1039/d4cc03501a.

(66) Dolmans, D. E. J. G. J.; Fukumura, D.; Jain, R. K. Photodynamic Therapy for Cancer. *Nat Rev Cancer* **2003**, *3* (5), 380–387.

(67) Wang, F. X.; Chen, M. H.; Lin, Y. N.; Zhang, H.; Tan, C. P.; Ji, L. N.; Mao, Z. W. Dual Functions of Cyclometalated Iridium(III) Complexes: Anti-Metastasis and Lysosome-Damaged Photodynamic Therapy. *ACS Appl Mater Interfaces* **2017**, *9* (49), 42471–42481. https://doi.org/10.1021/acsami.7b10258.

(68) Brouwer, A. M. Standards for Photoluminescence Quantum Yield Measurements in Solution (IUPAC Technical Report)*. *Pure Appl. Chem.* **2011**, *83* (12), 2213–2228. https://doi.org/10.1351/PAC-REP-10-09-31.

(69) Xu, C.; Webb, W. W. Measurement of Two-Photon Excitation Cross Sections of Molecular Fluorophores with Data from 690 to 1050 Nm. *Journal of the Optical Society of America B* **1996**, *13* (3), 481–491. https://doi.org/10.1364/JOSAB.13.000481.

(70) de Reguardati, S.; Pahapill, J.; Mikhailov, A.; Stepanenko, Y.; Rebane, A. High-Accuracy Reference Standards for Two-Photon Absorption in the 680–1050 Nm Wavelength Range. *Opt Express* **2016**, *24* (8), 9053. https://doi.org/10.1364/oe.24.009053.